Journal Pre-proofs

Mechanical Properties Prediction of Injection Molded Short/Long Carbon Fiber Reinforced Polymer Composites Using Micro X-Ray Computed Tomography

Shenli Pei, Kaifeng Wang, Jingjing Li, Yang Li, Danielle Zeng, Xuming Su, Xianghui Xiao, Hui Yang

PII: S1359-835X(19)30481-6
DOI: https://doi.org/10.1016/j.compositesa.2019.105732
Reference: JCOMA 105732

To appear in: *Composites: Part A*

Received Date: 21 August 2019
Revised Date: 12 December 2019
Accepted Date: 12 December 2019

Mechanical Properties Prediction of Injection Molded Short/Long Carbon Fiber Reinforced Polymer Composites Using Micro X-Ray Computed Tomography

Shenli Pei[a], Kaifeng Wang[b,a1], Jingjing Li[a2], Yang Li[c], Danielle Zeng[c], Xuming Su[c], Xianghui Xiao[d], Hui Yang[a]

[a]Department of Industrial and Manufacturing Engineering, Pennsylvania State University, University Park, PA 16802, USA

[b]Key Laboratory of Mechanism Theory and Equipment Design of Ministry of Education, Tianjin University, Tianjin 300354, CHN

[c]Research and Innovation Center, Ford Motor Company, Dearborn, MI 48124, USA

[d]National Synchrotron Light Source II, Brookhaven National Laboratory, Upton, NY 11973, USA

Abstract

This paper addresses the challenge of reconstructing nonuniformly orientated fiber-reinforced polymer composites (FRPs) with three-dimensional (3D) geometric complexity, especially for fibers with curvatures, and proposes a framework using micro X-ray computed tomography (μXCT) images to quantify the fiber characteristics in 3D space for elastic modulus prediction. The FRP microstructure is first obtained from the μXCT images. Then, the fiber centerlines are efficiently extracted with the proposed fiber reconstruction algorithm, i.e., iterative template matching, and the 3D coordinates of the fiber centerlines are adopted for quantitative characterization of the fiber morphology. Finally, Young's modulus is predicted using the Halpin-Tsai model and laminate analogy approach, and the fiber configuration averaging method with the consideration of the fiber morphology. The new framework is demonstrated on both injection-molded short and long carbon

[1] Corresponding author: Tel: 86-13821343256
E-mail address: wangkf@tju.edu.cn
Postal address: 220 Building 37th, Tianjin University, Jinnan District, Tianjin 300354, CHN.
[2] Corresponding author: Tel: 1-814-863-1300 Fax: 1-814-863-4745
E-mail address: jul572@psu.edu
Postal address: 310 Leonhard Building, University Park, PA 16802, USA

fiber-reinforced polymer composites, whose fiber morphology and predicted mechanical properties are validated through previous pyrolysis and quasi-static tensile tests, respectively.

Keywords: *Carbon fiber reinforced polymer composite; Micro-X-ray computed tomography; B. Mechanical properties; A. Microstructures*

1. Introduction

Micro X-ray computed tomography (μXCT), as a typical nondestructive imaging technique, has demonstrated its advantages to explore the detailed three-dimensional (3D) internal structure of carbon fiber-reinforced polymer (CFRP) composites including unidirectional, laminated, injection-molded, and chopped-fiber composites [1–5]. By leveraging the variation of X-ray attenuations owing to the differences in density and atomic number, the captured microscale XCT images can unveil the composite constituents, e.g., fibers, matrix, and defects [3–8], where the high-density material (e.g., fibers) appears brighter than the low-density material (e.g., matrix). At present, μXCT is effectively used to understand the initiation and evolution of damage and to determine the *in-situ* fracture mechanics of CFRP composites [4,6,9–14]. However, only limited quantitative image analyses of μXCT images have been reported for non-uniformly orientated CFRP composites, especially for those consisting of curved fibers. This is because the appropriate post-image processing algorithms such as the Bayesian inference theory-based and machine learning-based approaches depend considerably on the image quality and material nature [15–17]. Emerson *et al.* [18] proposed a dictionary-based probabilistic segmentation technique to indicate the likelihood of a voxel belonging to a fiber or the matrix, which required the user’s inputs, including dictionary patch size and representative labeled patches to identify fiber centroid from 2D images. In the revised version of this approach, Emerson *et al.* [19] reduced the computation time for training the supervised learning model and the probabilistic segmentation phase and improved the fiber centerline tracking using a bidirectional approach. This approach was presented on unidirectional carbon fiber. Czabaj *et al.* [7] proposed a two-step algorithm based on 2D template matching for fiber identification followed by a Kalman filtering approach for tracking. Creveling *et al.* [20] proposed an extension to this approach, replacing the manually picked templates for synthetically created 2D fiber templates to identify the fibers and determine the fiber centroids and the fiber diameters. This approach was demonstrated on laminate CFRP composites with a stacking sequence of [+45°/-60°/+60°]. Sencu *et al.* [21] proposed a Bayesian inference theory-based approach to segment fibers and track the fiber centerlines, in which the size of the kernel and convolution factors are determined semi-empirically by user's visual inspection. The use of the local inference model to track fiber centerlines required a series of tuning for different fiber shifts completed by the user. The proposed approach was demonstrated on multidirectional laminate CFRP composites with a stacking sequence of [+45°/90°/-45°/0°] by separating 90° ply from the rest of the material and treating it as 0° UD carbon fibers through the rotation.

Discontinuous FRPs exhibit complex microstructures owing to a variety of fiber lengths, orientations, and curvatures. There is an urgent need to develop new analytical methods for the characterization and analysis of individual fiber segments. Agyei *et al.* [22] proposed a framework that consisted of a four-step sequential 2D segmentation approach and a 3D volume rendering algorithm to generate a 3D morphology that represented the microstructure for short fiber-reinforced composites. In this four-step sequential 2D segmentation approach, the researchers adopted iterative sharpening, iterative marker-controlled watershed, case-by-case comparison for highly clustered out-of-plane fibers, and replacement of segmented regions with fitted ellipses to achieve an optimum segmentation. The 3D volume rendering approach refined the microstructure by separating connected fibers and stitching over-segmented fibers. The proposed framework was demonstrated on an injection molded glass fiber reinforced polymer composite. Hessman *et al.* [23] proposed an iterative single fiber segmentation and merging approach to obtain fiber microstructural characteristics such as orientation, location, radius and length directly from the scanned images. This approach was implemented on artificial μCT data, which achieved a higher quality compared to the commercial software, though the approach neglected the possible curvatures. The challenges of reconstructing non-uniformly orientated CFRP composites with curved fibers are the inherent variabilities from the material owing to orientation and curvature variants, the computational complexity of the 3D image data, and tracking of a curved fiber from a congested fiber system in a 3D space. Therefore, there is a need to develop a suitable segmentation and tracking algorithm to extract the internal structures of CFRP composites, considering the fiber orientation and fiber curvature.

Image-based modeling has recently demonstrated the advantages of using XCT images to generate a realistic finite element mesh for material behavior modeling [24–26]. However, the process of extracting and replicating complex geometry for a numerical model requires more intensive computation than models using idealized representative volume elements [17]. Thus, establishing a relationship between the image-based spatial statistics and material properties at a different length scale with a less computational effort is desired. A number of attempts have been made to predict the mechanical behavior of fiber-reinforced composites [27–30]. Huang proposed a micromechanical strength theory to calculate the mechanical properties of unidirectional fiber composites [28]; however, complex fiber morphologies were not considered. Nguyen *et al.* employed the Eshelby's equivalent inclusion method to calculate a material's overall stiffness using an orientation averaging approach, where the fiber orientation and fiber length distributions were measured from 2D microscopic images [29]. Kunc *et al.* proposed a fiber configuration with curvatures and extended the orientation averaging approach to configuration averaging to account for the fiber curvature. The statistical distributions of fiber length and fiber curvature were measured separately, in which the fiber length distribution was achieved by pyrolysis tests, and the fiber curvature distribution was measured from XCT images. The corresponding fiber morphology distribution considering both fiber length and fiber curvature was then generated by a random number generator to pair these two distributions. This approach reported an error of 15% in the experimental results [30]. The realistic 3D spatial statistics of the material microstructure must be considered when implementing mechanical property prediction models in order to obtain an accurate estimation of a material's mechanical properties,

The present study demonstrates a combined computational and analytical framework for image-based reconstruction, quantitative morphological characterization, and a mechanical prediction of short and long fiber reinforced polymer composites with non-uniformly oriented fibers. The framework consists of a non-destructive imaging technique (μXCT) for capturing the internal microstructures, the proposed reconstruction algorithm (iterative template matching) for extracting and tracking fiber centerlines, and spatial statistic characterization of the 3D fiber geometric properties (i.e., fiber volume fraction, length, orientation, and curvature distributions) for elastic property calculations such as Young's modulus prediction. The framework leverages the benefits of μXCT to obtain a realistic internal 3D microstructure and the advantages of the proposed iterative template matching approach that account for non-uniform fiber orientation, fiber curvatures, and congested fiber systems to improve the mechanical property estimation and provide the spatial characterization and mechanical properties of the material. The proposed framework is applied to short CFRP (SCFRP) composites with straight fibers and long CFRP (LCFRP) composites with curved fibers. The reported computational results are validated through quasi-static tensile [31] and pyrolysis tests [32].

2. Experimental Procedure and Methodology of CFRP reconstruction

2.1 Materials and Experimental Procedure of μXCT

The μXCT was performed on the micro-tomography beamline 2-BM-A at the Argonne National Laboratory to obtain the internal microstructure of the materials. In this study, two CFRP composites were scanned separately, and the material composition and mechanical property are listed in Table 1. The µXCT scans were performed over a rotation of 180° using a beam energy of 27 keV with an exposure time of 0.05 seconds per image. Each scan captured more than 1400 2D grayscale images with a dimension of 2560 × 2560 pixels at a voxel size of 1.3 µm, so the ratio between the fiber diameter to the number of pixels is 5-6. The constituents of the CFRP composites (i.e., fiber and matrix) were differentiated through variations in X-ray absorption. The initial data conversion from the raw data to grayscale images was performed using TomoPy, a well-established open-source Python package designed for processing and reconstructing tomographic data [34]. Interested readers can refer to [4] for further details of the post-experiment image conversion.

Table 1. Material Composition and Mechanical Property of CFRP composites

Composite	Matrix	Fiber weight fraction (%)	Avg. Fiber Length (µm)	Avg. Fiber Diameter (µm)	Avg. Young's Modulus (GPa)
Short CFRP	Polyamide 6/6	40[a]	104.8 (Core Layer)[a] 117.9 (Skin Layer)[a]	7	13.8 (Core Layer)[a] 21.9 (Skin Layer)[a]
Long CFRP	PA 66	40[b]	-	7	29.3[b]

[a]Taken from ref [8]
[b]Taken from ref [33]

2.2 Fiber Reconstruction using Iterative Template Matching

The complete workflow of the proposed iterative template matching reconstruction algorithm is displayed in Figure 1; the algorithm is divided into three sections and implemented in Matlab®. In the first step (initialization), a global segmentation method, Otsu's multilevel thresholding [35], is employed to separate the fibers from the matrix as indicated in Figure 1b, where the input images are grayscale image stacks obtained from µXCT as presented in Figure 1a. In the second step, the local intensity gradient segmentation further isolates the fiber voxels based on the 3D grayscale intensity gradient changes by removing the edge voxels. The remaining voxels are skeletonized to preserve the morphological shape of the fibrous structure and to represent fiber centerlines, as illustrated in Figure 1c. In the third step, fiber tracking, template matching [7,20,21,36], and a local fiber-tracking scheme are performed to determine and assign the fiber centerlines for the individual fibers throughout the volume while removing voxels that belong to fibers that are in contact. One of the outputs of the reconstruction algorithm is a labeled volume in which voxels with the same label represent the centerline of an individual fiber. A detailed description of each step is presented in the following subsections.

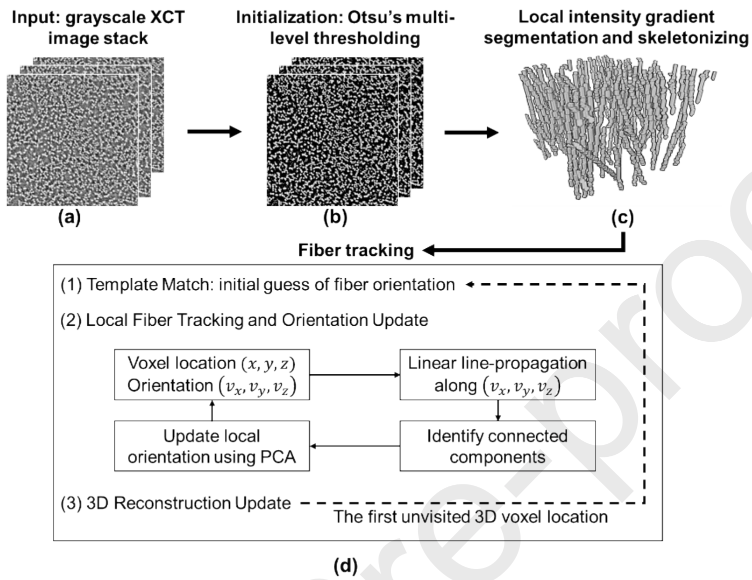

Figure 1. The flow chart of the iterative template matching algorithm: (a) grayscale image stacks as data input, (b) segmentation of 3D images using Otsu's multilevel thresholding, (c) skeletonized volume of further segmentation using local intensity gradient segmentation, and (d) fiber tracking.

2.2.1 *Initialization*

To generate the initial isolation of the fibers, the original grayscale XCT 3D images (Figure 2a) are processed with Otsu's method [35] which coarsely clustered the constituents in the composite into different groups by minimizing the voxel intensity variance of each group and maximizing the voxel intensity variance across groups. A representative of grayscale intensity histogram, presented in Figure 2b, has a probability distribution containing three peaks and two valleys, where three peaks are located approximately at grayscale values of 100, 190, and 250, and two valleys are located approximately at grayscale values of 175 and 145. Although fibrous composites can be considered as a biphasic material, a single threshold level separating the voxels into two groups may not be sufficient to remove matrix voxels, as demonstrated in Figure 2c, where a one-level threshold value of 139 is adopted, and the voxels belonging to the brighter grayscale intensity class are retained with the original grayscale intensity. Figures 2c and 2d present the two-level (174) and three-level thresholding (195) of the original image, respectively, and voxels in the brightest grayscale intensity class are retained with the original grayscale intensity. Figure 2e shows that the three-level thresholding leads to an over truncation, whereas the one-level thresholding is not quite effective in removing matrix voxels as presented in Figure 2c. Two-level thresholding results in the best global segmentation with a value located at one of the local minima of the grayscale intensity histogram, illustrated in Figure 2b. It should be noted that a small number of gray-colored voxels, representing the polymer matrix and fiber edges, are retained because Otsu's method is a global thresholding method and cannot differentiate polymer voxels with a similar grayscale intensity to that of the fiber voxels.

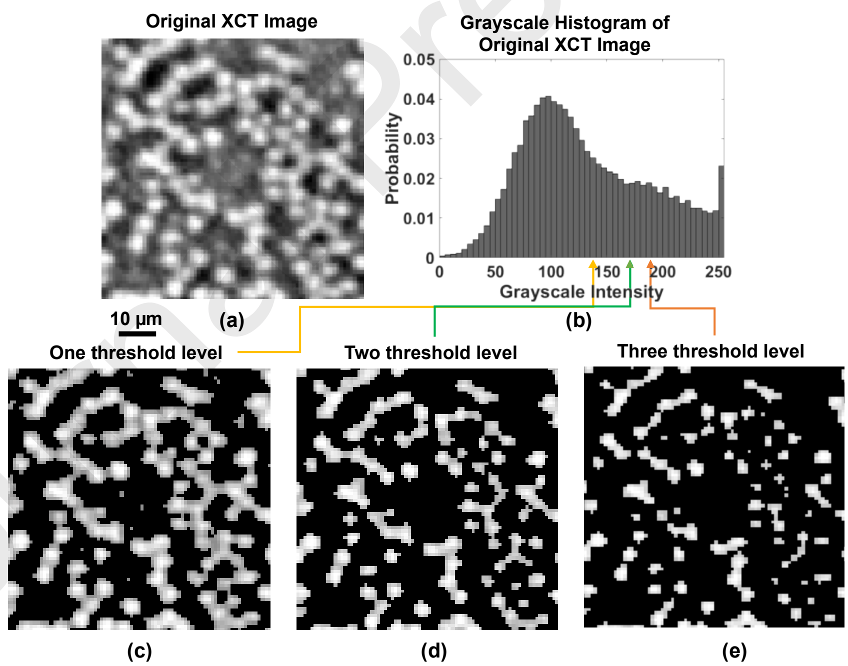

Figure 2. (a) Original XCT image, (b) grayscale intensity histogram of the original XCT image, (c) the filtered image after single-level thresholding, (d) the filtered image after two-level thresholding, and (e) the filtered image after three-level thresholding.

2.2.2 *Local intensity gradient segmentation*

The initial coarsely segmented grayscale volumetric images then undergo a local intensity gradient segmentation to remove fiber edge voxels through the calculation of the absolute grayscale intensity gradients in the longitudinal direction (LD), transverse direction (TD), and normal direction (ND), i.e., I'_{LD}, I'_{TD}, and I'_{ND}, where $I(x,y,z)$ represents the voxel intensity at the location (x,y,z) and the tilde symbol and subscripts indicate the intensity gradients in the corresponding directions. The grayscale intensities of fiber voxels change gradually with higher grayscale intensities at the fiber centers and lower grayscale intensities at fiber edges. Hence, the fiber edge voxels have a more positive or negative grayscale intensity gradient. As presented in Figure 3, the typical probability distributions of the absolute voxel-intensity gradients of an image volume with dimensions of 400 × 200 × 200 voxels (LD × TD × ND) naturally contain a thresholding criterion distinguishing edge voxels from fiber voxels, where the edge voxels have a considerably larger absolute intensity gradient than fiber voxels. Voxels with near-zero grayscale intensity gradients in all three directions (i.e., LD, TD, and ND) are retained as presented in Figure 3d, resulting in a separation of a few connected fibers as illustrated by yellow arrows. The segmented volume is then skeletonized to obtain voxels representing the centerline of each fiber as displayed in Figure 1c.

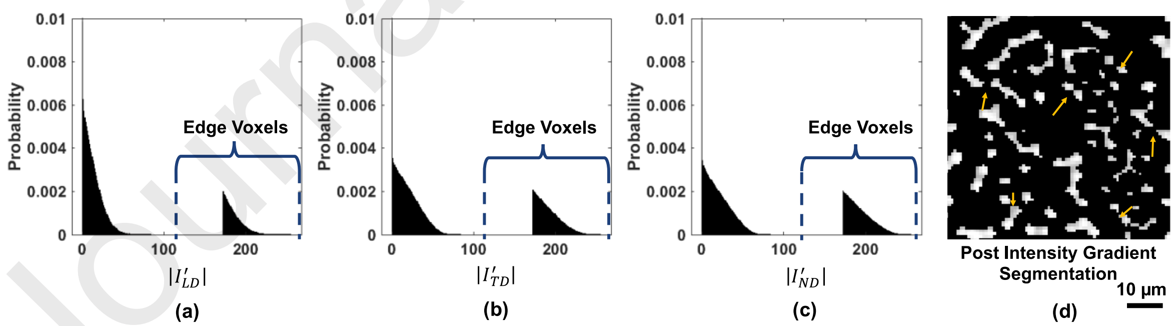

Figure 3. Probability distributions of absolute intensity gradients in (a) LD, (b) TD, (c) ND using the extracted volume of 400 × 200 × 200 voxels in SCFRP composite. (d) a representative µXCT image after intensity gradient segmentation.

2.2.3 *Fiber Tracking*

The skeletonized volume is converted to a set of sorted 3D voxel locations (denoted as $S = \{s\}$)

for fiber tracking, and these voxel locations are sorted according to their spatial locations in the directions of LD and ND. The set, *S*, designates coordinates of approximate locations for fiber centers. A small portion of misidentified voxel locations is related to touching fibers in the congested fiber systems, where the proportion of misidentified voxel locations is determined by comparing the total numbers of voxel locations of the skeletonized volume and the labeled volume. The average difference measured in this study is 6.6 ± 1.1%, which is less than 8%. The fiber-tracking algorithm is developed based on 3D template matching to estimate orientations of fibers, and a local fiber tracking is then implemented to obtain robust fiber tracks, through which voxels belonging to the same fiber are identified. Although template matching is a well-established technique in image processing using the morphology of a template to identify similar parts in a larger target image, the accuracy of the detection depends on the selection of templates [7]. A brief summary is presented here for clarity; the detailed formation and description can be found in [36]. Template matching calculates the normal cross-correlation (NCC) score for each voxel in the skeletonized volume using the following expression:

$$NCC(u,v,w) = \frac{\sum_{u,v,w}[I(u,v,w)-\bar{I}][T(u-u',v-v',w-w')-\bar{T}]}{\sqrt{\sum_{u,v,w}[I(u,v,w)-\bar{I}]^2\sum_{u,v,w}[T(u-u',v-v',w-w')-\bar{T}]^2}}, \qquad (1)$$

where *I(u,v,w)* is the grayscale intensity of location *(u,v,w)* with size M × N × L (i.e., the dimension of the volume for reconstruction); *T(u-u', v-v',w-w')* is the grayscale intensity of the template with size m × n × l (i.e., the dimension of the template), which is shifted by *u'* voxels in the LD, *v'* voxels in the TD, and *w'* voxels in the ND; $\bar{I}$ is the average grayscale intensity in the m × n × l region centered at *(u,v,w)*; $\bar{T}$ is the average grayscale intensity of the template. All summations in Eq. 1 are performed over the m × n × l and a perfect positive (negative) correlation reveals an NCC value of “1” (“-1”).

Numerous CFRP composites contain fibers in different orientations; therefore, one single template cannot sufficiently nor accurately estimate fiber orientation, and a set of templates based on a short straight fiber, presented in Figure 4a, is preferred. The fiber diameter of the template is set to be six voxels, which is estimated by visual inspection from the µXCT images. The cross-section of a short straight fiber template is emulated using a Gaussian filter, as presented in Figure 4b, which ensures the highest grayscale intensity at the fiber centerline and a gradual intensity decrease from the center to the edge. Templates with different fiber orientations are generated by rotating the initial short fiber template around the ND-axis from -90° to +90° with a 10° increment, and then the TD-axis from -90° to +90° with a 10° increment to ensure the templates are robust against all fiber orientations. The NCC score for a voxel location, *s*, is calculated according to Eq. 1, and the estimated orientation is chosen by selecting the orientation corresponding to the highest NCC score.

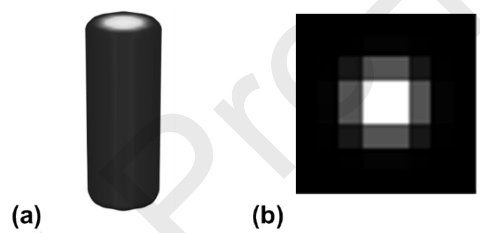

Figure 4. (a) Initial template of the short straight fiber and (b) cross-section of the template.

To determine the appropriate length of the fiber template, a preliminary study was performed to examine the orientation estimation accuracy and computational time for the fiber templates with a length of 8, 16, and 32 voxels. The tested volume was synthesized containing 110 straight fibers with a length of at least 50 voxels and known orientations ranging from -90° to +90° with a 10° increment in both the ND-and TD-axes forming a uniform distribution for fiber orientation with a volume size of 200×100×100 voxels. The experiment was performed in Matlab® with an Intel® Core i7-8700 CPU at 3.20 GHz and 64.0 GB memory. The template with a fiber length of 32 voxels achieved the highest accuracy (98.9%) among all three cases with the longest computational time (approximately 10 min); the computational time and orientation estimation accuracy for the templates with fiber lengths of 8 and 16 voxels were approximately 2.5 min, 78.9%, and approximately 5 min, 94.7%, respectively. When considering both orientation estimation accuracy and computational cost, the template with a fiber length of 16 voxels was selected. The fiber template was then tested on a synthesized volume containing 121 curved fibers, where 109 of the curved fibers were correctly identified and all of the misidentified fibers had a fiber length shorter than that of the fiber template, indicating that the proposed template can identify both straight and curved fibers.

For a reasonably sized 3D image, computing the NCC scores for all voxel locations can be computationally expensive. Therefore, a fiber-tracking algorithm using a linear line propagation-approach [37] is implemented to identify voxel locations along the estimated orientation. As described below, the NCC scores do not have to be computed at these locations, thereby reducing the amount of computation time. The local orientation is updated using the identified voxel locations for fiber tracking in the next iteration. Figure 5 demonstrates the local fiber tracking and orientation update algorithm in 2D space (e.g., TD-LD plane), where the grid represents each pixel in the 2D image (i.e., search space), and "*X*" is the pixel of the fiber centerline, whose pixel location is an element of *S*. In Figure 5a, an "*X*" in a blue box represents the current pixel that is being tracked, and the estimated fiber orientation calculated from the template matching step is presented as a blue dashed line. For a given orientation, a linear line propagation can be used to detect other locations aligned with the estimated orientation, which forms a tracking path. The length of the linear line propagation is the same as the length of a fiber template (i.e., 16 voxels). In the example illustrated in Figure 5a, a short linear line propagation length is implemented for demonstration. Pixels on the linear line propagation (Figure 5a) are shaded in grey, which narrows the search space, and only four "*X*"s, indicated in red, are selected for local orientation update. These four locations are then used for image dilation to obtain the connected centerlines displayed in the gray-shaded boxes in Figure 5(b). The localized orientation is computed through principal component analysis (PCA) of the selected coordinates. The eigenvector corresponding to the largest eigenvalue indicates the direction of the largest spatial variation (i.e., the fiber orientation), which is presented by a new blue dotted line in Figure 5c. The endpoint of the linear line propagation becomes the new starting point for the tracking presented by the blue box in Figure 5c. This tracking procedure continues until one of the terminating conditions is satisfied. The terminating process is initiated when less than three voxel locations are identified on the tracking path. The algorithm will extend the linear line propagation for another length of 16 voxels to enlarge the search region. In the first scenario, there are less than three locations identified, so the tracking procedure is terminated immediately. The rational of this termination condition is that the minimum required number of locations for PCA in 3D is three. In the second scenario, more than three locations are identified, and the PCA captures an abrupt change in fiber orientation. This implies that the tracking algorithm identifies another nearby fiber with different orientations. After the termination of the tracking procedure, a unique label is then assigned to the locations representing the fiber centerline, excluding locations identified during the termination process. The labeled voxel locations are noted as visited locations, and a new search will be initiated at the first unvisited voxel location of the set *S* until all voxel locations are visited. For congested fiber systems, the change of local fiber orientation is monitored. An abrupt change in local fiber orientation is identified as a possible crossing fiber. The tracking procedure continues by extending the linear line propagation along the fiber orientation determined from the previous iteration. Voxels identified only in the second linear line extension are then used for computing local orientation. When a smooth orientation change is identified, voxels in the region of fiber intersection are then interpolated, and the tracking procedure continues. In contrast, an abrupt orientation change will trigger the second terminating condition. By tracking each fiber in segments, the gradual local orientation change for fibers with curvatures is identified and the global fiber orientation and fiber curvature are then characterized (see Section 2.3.1).

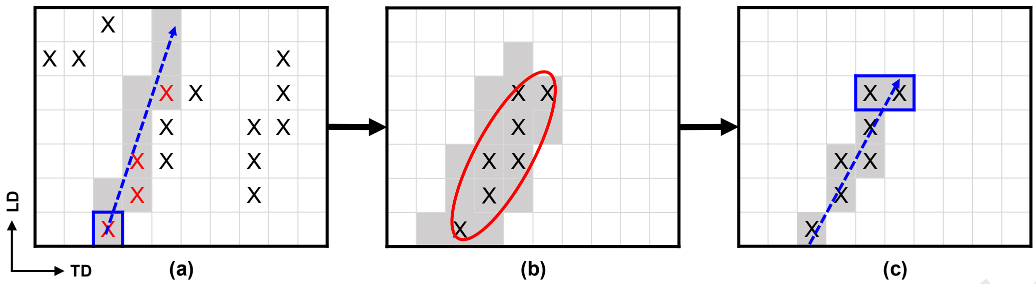

Figure 5. Schematics of local fiber tracking and orientation update where “X”s present location of fiber centers: (a) linear line propagation of orientation estimated from template matching in blue dotted line and selected coordinates in red, (b) identification of connected components shaded in gray and PCA in red oval, and (c) local orientation update in dotted blue arrow and new starting point update outlined in blue box.

2.3 Description of Microstructure

To consider the effect of fiber curvatures on the mechanical properties of the composite material, Kunc *et al.* introduced a configuration to describe curved fibers [30], where the ensemble of curved fibers with different morphologies can be characterized via tensor representation by summarizing the probability density function of each configuration. Using the proposed fiber configuration and configuration averaging approach, this paper extends the existing stress-strain constitutive equations [27, 30] to calculate the stiffness tensor with the consideration of the local fiber length and local fiber curvature distributions simultaneously, thereby providing a prediction of Young’s modulus. The following subsections present detailed descriptions of fiber configuration, tensor representation, and stiffness tensor.

2.3.1 Configuration of A Single Fiber

A brief description of a single fiber configuration with and without curvature is presented in this subsection. For a straight fiber, it can be assumed that the fibers are rigid cylinders with a uniform diameter, as presented in Figure 6a, where the centroid of the fiber coincides with the origin of the coordinate system. The fiber orientation is defined by a unit vector, $\vec{\boldsymbol{p}}$, along the centerline of the fiber, which can also be represented by the angles (θ, φ) defined in Figure 6(a) with the spherical coordinate system. The components of the vector $\vec{\boldsymbol{p}}$ can be written as follows:

$$\vec{\boldsymbol{p}} = (p_{LD}, p_{TD}, p_{ND}) = (\cos\theta, \quad \sin\theta\cos\varphi, \quad \sin\theta\sin\varphi). \tag{2}$$

For a curved fiber, Kunc *et al.* [30] presented a fiber coordinate system $(\vec{\boldsymbol{p}}, \vec{\boldsymbol{q}}, \vec{\boldsymbol{s}})$ through transformation of three Euler angles, following the Euler ZYX (i.e., LD-ND-TD) convention, where rotation is performed about an LD of angle α, then about the new ND (i.e., ND') of angle β, and lastly about the new TD (i.e., TD'') of angle γ, as illustrated in Figure 6b. The defined fiber coordinate system is presented in Figure 6c, where the centroid of the fiber coincides with the origin of the fiber coordinate system $(\vec{\boldsymbol{p}}, \vec{\boldsymbol{q}}, \vec{\boldsymbol{s}})$. Hence, $\vec{\boldsymbol{p}}$ is tangent to the fiber centerline at the fiber centroid, $\vec{q}$ is in the direction of the curvature radius, and $\vec{s}$ is normal to both $\vec{\boldsymbol{p}}$ and $\vec{\boldsymbol{q}}$. The components of vectors $\vec{\boldsymbol{p}}$ and $\vec{\boldsymbol{q}}$ can be written as follows:

$$\vec{\boldsymbol{p}} = (p_{LD}, p_{TD}, p_{ND}) = (-\sin\beta, \quad \cos\alpha\cos\beta, \quad \sin\alpha\cos\beta), \tag{3a}$$

$$\vec{\boldsymbol{q}} = (q_{LD}, q_{TD}, q_{ND}) = (\cos\beta\sin\gamma, \quad \cos\alpha\sin\beta\sin\gamma - \sin\alpha\cos\gamma, \quad \sin\alpha\sin\beta\sin\gamma - \cos\alpha\cos\gamma). \tag{3b}$$

The geometric shape of a single fiber is defined by two dimensionless parameters, namely the aspect ratio, $\xi = L/d$, and the curvature ratio, $\eta = L/R$, where L is the length of the fiber, d is the diameter of the fiber, and R is the radius of the curvature at the centroid of the fiber. The limiting case of a straight fiber implies $\eta = 0$.

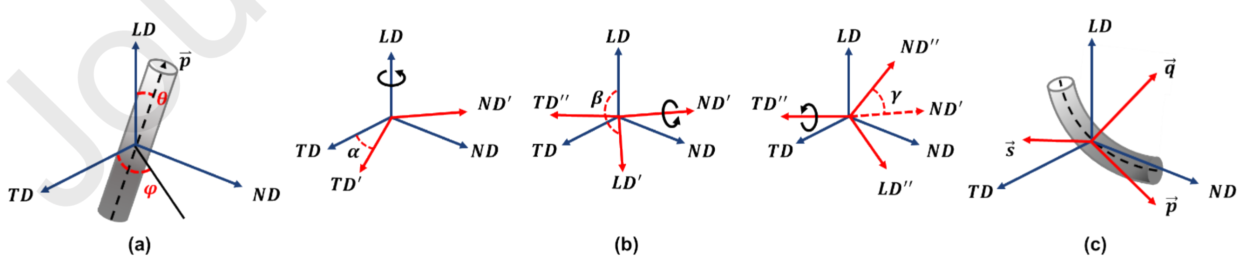

Figure 6. Configurations of (a) straight cylindrical fiber, (b) Euler ZYX convention, and (c) fiber with curvature.

To estimate fiber morphology from the reconstructed volume, the voxel locations of one fiber are used, where the mathematical definition of centroid is applied to determine the location of fiber centroid. The orientation vector is then calculated by extracting the first principal component of the fiber centroid voxel location and its neighboring voxel locations that are within a distance of 8 voxels (i.e., half of the fiber template length) from the centroid. The fiber curvature vector is the unit vector from the fiber centroid to the center of a fitted a sphere with the least-square approach, which is computed using all voxel locations belonging to a fiber.

2.3.2 Tensor Representation for An Ensemble of Fibers

For a given material containing fibers with different configurations, the morphology of an ensemble of fibers with their Euler angles (α, β, γ) and shape parameters (ξ,η) can be represented by the probability density function $\psi_C(\alpha,\beta,\gamma,\xi,\eta)$. The probability of finding a fiber with a given configuration, e.g., (α_1,β_1,γ_1,ξ_1,η_1), is defined by [30]:

$$\begin{aligned} &P(\alpha_1 \le \alpha < \alpha_1 + d\alpha, \beta_1 \le \beta < \beta_1 + d\beta, \gamma_1 \le \gamma < \gamma_1 + d\gamma, \xi_1 \le \xi < \xi_1 + d\xi, \eta_1 \le \eta < \eta_1 + d\eta) \\ &\quad = \psi_C(\alpha_1,\beta_1,\gamma_1,\xi_1,\eta_1)\cos\beta_1\, d\alpha d\beta d\gamma d\xi d\eta, \end{aligned} \tag{4}$$

which is normalized as the following:

$$\int_{\eta=0}^{\infty}\int_{\xi=0}^{\infty}\int_{\gamma=0}^{2\pi}\int_{\beta=-\pi/2}^{\pi/2}\int_{\alpha=0}^{2\pi}\psi_C(\alpha,\beta,\gamma,\xi,\eta)\cos\beta d\alpha d\beta d\gamma d\xi d\eta = 1. \tag{5}$$

Assuming the independence between the Euler angles and shape parameters, ψ_C can be separated into rotation probability density function (ψ_R), and shape probability density function (ψ_S), and can be written as $\psi_C = \psi_R(\alpha, \beta, \gamma)\psi_S(\xi, \eta)$. Using even-order tensors to describe the rotation component can reduce the computational costs and present a compact representation of the ensemble [38]. Advani and Tucker [38] suggested that only second- and fourth-order tensors are required to estimate the material fourth-order stiffness tensor (i.e., [C_{ijkl}]); the second- and fourth-order orientation tensors (i.e., [a_{ij}] and [a_{ijkl}]), curvature tensors (i.e., [b_{ij}] and [b_{ijkl}]), and mixed tensor (i.e., [c_{ijlk}]) are described as follows [30]:

$$\boldsymbol{a_2} = [a_{ij}] = \int_{\beta=-\pi/2}^{\pi/2}\int_{\alpha=0}^{2\pi} p_i p_j \psi(\alpha,\beta)\cos\beta\, d\alpha d\beta, \quad i,j = LD, TD, ND, \tag{6a}$$

$$\boldsymbol{b_2} = [b_{ij}] = \int_{\gamma=0}^{2\pi}\int_{\beta=-\pi/2}^{\pi/2}\int_{\alpha=0}^{2\pi} q_i q_j \psi_R(\alpha,\beta,\gamma)\cos\beta\, d\alpha d\beta d\gamma, \quad i,j = LD, TD, ND, \tag{6b}$$

$$\boldsymbol{a_4} = [a_{ijkl}] = \int_{\beta=-\pi/2}^{\pi/2}\int_{\alpha=0}^{2\pi} p_i p_j p_k p_l \psi(\alpha,\beta)\cos\beta\, d\alpha d\beta, \quad i,j,k,l = LD, TD, ND, \tag{6c}$$

$$\boldsymbol{b_4} = [b_{ijkl}] = \int_{\gamma=0}^{2\pi}\int_{\beta=-\pi/2}^{\pi/2}\int_{\alpha=0}^{2\pi} q_i q_j q_k q_l \psi_R(\alpha,\beta,\gamma)\cos\beta\, d\alpha d\beta d\gamma, \quad i,j,k,l = LD, TD, ND, \tag{6d}$$

$$\boldsymbol{c_4} = [c_{ijkl}] = \int_{\gamma=0}^{2\pi}\int_{\beta=-\pi/2}^{\pi/2}\int_{\alpha=0}^{2\pi} p_i p_j q_k q_l \psi_R(\alpha,\beta,\gamma)\cos\beta\, d\alpha d\beta d\gamma, \quad i,j,k,l = LD, TD, ND, \tag{6e}$$

where the subscripts "2" and "4" present the second- and fourth-order tensors, $p_{i,}$ and q_i are components of the orientation vector $\vec{\boldsymbol{p}}$ and the curvature vector $\vec{\boldsymbol{q}}$, and $\psi(\alpha,\beta) = \int_{\gamma=0}^{2\pi}\psi_R(\alpha,\beta,\gamma)$ $d\gamma$. For an ensemble of fibers with known fiber orientation and curvature vectors, their Euler angles, (α, β, γ), can be calculated through Eq. 3, and the statistical distribution of the Euler angles is summarized to formulate the probability density function of $\psi_R(\alpha,\beta,\gamma)$ and $\psi(\alpha,\beta)$ with Eq. 4. The tensors in Eq. 6 are calculated accordingly where p_i and q_i values are determined by the Euler angles (α, β, γ). Hence, the tensor representation considers the statistical distribution of the fiber orientation and fiber curvature, and fourth-order tensors are adequate to capture variations within a distribution [38].

2.3.3 Stiffness Tensor for An Ensemble of Fibers using Configuration Averaging

The fourth-order stiffness tensor, C_{ijkl}, of composites containing curved fibers, is extended from the orientation averaging approach that considers only a_{ij} and a_{ijkl}, and is formulated as [30]:

$$C_{ijkl} = \mu(\delta_{ik}\delta_{jl} + \delta_{il}\delta_{jk}) + \lambda\delta_{ij}\delta_{kl} + k_{p_2}(a_{ij}\delta_{kl} + a_{kl}\delta_{ij}) + k_{q_2}(b_{ij}\delta_{kl} + b_{kl}\delta_{ij}) + 2\mu_1 (a_{jl}\delta_{ik} + a_{jk}\delta_{il} + a_{ik}\delta_{jl} + a_{il}\delta_{jk}) + 2\mu_2(b_{jl}\delta_{ik} + b_{jk}\delta_{il} + b_{ik}\delta_{jl} + b_{il}\delta_{jk}) + k_{p4}a_{ijkl} + k \; {}_{ijkl} + k_{s4}(c_{ijkl} + c_{klij}), \; i,j,k,l = LD, TD, ND, \tag{7}$$

where δ is the Kronecker delta and μ, λ, k_{p_2}, k_{q_2}, μ_1, μ_2, k_{p4}, k_{q4}, and k_{s4} are material constants with the consideration of the shape probability density function, $\psi_S(\xi,\eta)$ [30] using the configuration averaging method:

$$\bar{n} = \int_{\xi=0}^{\infty}\int_{\eta=0}^{\infty} n(\xi,\eta)\psi_S(\xi,\eta)d\xi d\eta, \tag{8}$$

where $\bar{n}$ represents all nine material constants in Eq. 7, and $n(\xi,\eta)$ is extended from the material constants for straight fibers, namely μ_s, μ_0, λ_s, ζ_2, and ζ_4, obtained from the Halpin–Kardos [39] and Halpin–Tsai [40] equations with Young's modulus (E) and Poisson's ratio (v). Interested readers should refer to [40] and [30] for a detailed calculation of the material constants for materials with straight fibers and curved fibers, respectively. For the limiting case of $\eta = 0$ (i.e., $R = \infty$ for a straight fiber), Eq. 7 is reduced to the stiffness tensor for a transversely isotropic material, which is written as the following:

$$C_{ijkl} = \mu_s(\delta_{ik}\delta_{jl} + \delta_{il}\delta_{jk}) + \lambda_s\delta_{ij}\delta_{kl} + \zeta_2(a_{ij}\delta_{kl} + a_{kl}\delta_{ij}) + (\mu_0 - \mu_s)(a_{jl}\delta_{ik} + a_{jk}\delta_{il} + a_{ik} + \zeta_4 a_{ijkl}. \tag{9}$$

3. Results and Discussion

The following demonstrates the application of the proposed framework using the non-destructive image-based technique to obtain the microstructure and mechanical property prediction of Young's modulus for short CFRP (SCFRP) and long CFRP (LCFRP) composites. The reconstruction and analytical results (e.g., fiber orientation and Young's modulus) are discussed and compared with the experimental results.

3.1 Short CFRP (SCFRP) composite with straight fibers

This research examined a SCFRP composite manufactured by PolyOne Corp. consisting of 40 weight percent (wt%) carbon fibers and Polyamide 66 as the polymer matrix was examined; this is a special case of an injection-molded CFRP composite having short and straight carbon fibers. Each dogbone SCFRP sample was machined from the as-received sheet, where the LD of the sample was aligned with the mold fill direction (i.e., the LD of the plaque), and the gauge dimension was 10 mm × 1.8 mm × 2.5 mm (LD × TD × ND, i.e., length × width × thickness). The fiber volume fraction and fiber length distributions were measured in reference [8] from the μXCT images and a pyrolysis experiment, where the reported values from the second approach were adopted as a validation for this study. The Young's modulus of the SCFRP composite, measured through tensile tests reported in [8], was used to validate the calculated modulus obtained in this study.

The original μXCT image, displayed in Figure 7, indicates that this material has a skin-core-skin structure, where more fibers in both skin layers are aligned in the LD than in the core layer. Detailed fiber characteristics in each layer were investigated through the proposed iterative template matching reconstruction algorithm, where three individual cuboids were extracted from the same layer with a size of 400 × 200 × 200 voxels (i.e., 0.520 mm × 0.260 mm × 0.260 mm) in the LD × TD × ND. Using the same computation configuration mentioned in section 2.2.3, the computation time for each volume was about 4 hours on average when three cores were used during the tracking phase, and each reconstructed volume contained an average of 1780 ± 198 fibers.

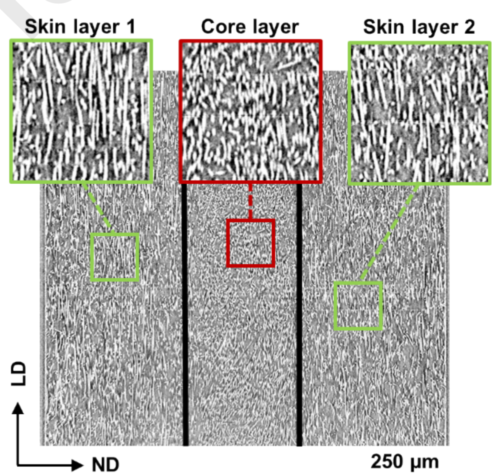

Figure 7. Representative 2D μXCT reconstruction of skin-core-skin structure in the LD/ND plane; TD is out of the plane.

The reconstructed volumes of each layer are displayed in Figure 8, where the fibers in all three volumes have a non-uniformly oriented distribution, and the fibers in the skin layers have tended to align in the LD (Figures 8a and 8c), the whereas fibers in the core layer have tended to align diagonally in the LD-TD plane (Figure 8b). Using the fiber configuration defined in Section 2.3.1, the average curvature ratio of the reconstructed volumes is 0.045 ± 0.009, implying that the radius of the curvature is, on average, 22.2 times the fiber length. Therefore, the fibers in the SCFRP composites are essentially straight fibers with an infinite radius of fiber curvature.

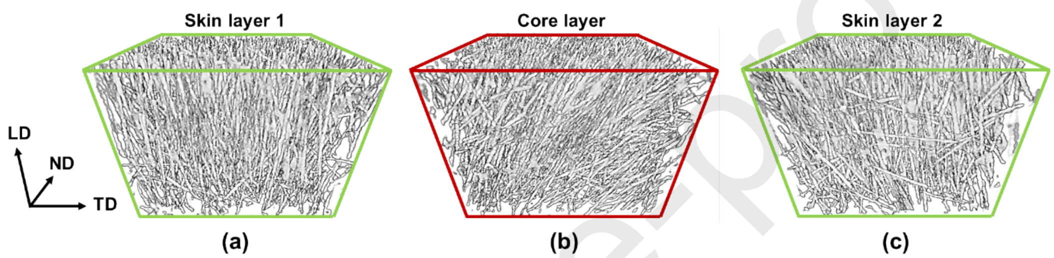

Figure 8. Representative reconstruction of SCFRP composite for (a) Skin layer 1, (b) Core layer, and (c) Skin layer 2.

Using the straight fiber configuration (Figure 6a), [8] detailed the fiber length distribution from the reconstructed volumes of Skin layer 1, Core layer, and Skin layer 2, where the average fiber length of Skin layer 1, Core layer, and Skin layer 2 was 117 ± 1 μm, 104 ± 4 μm, and 118 ± 2 μm, respectively. The fiber length distribution from the reconstructed volumes was validated via a pyrolysis experiment [8, 32]. Spatial representations of the color-coded fiber centerlines, with regard to the fiber angle between the fiber centerline and the LD direction, θ, are presented in Figure 9, where Figures 9a and 9b are color-coded fiber centerlines of the Core layer and Skin layer 1 cuboids, respectively. From visual observation, the fiber orientation distributions for these two layers are significantly different. The majority of the fibers in the Core layer have an orientation of 25°–30° (Figure 9b); whereas the majority of the fibers in the Skin layer 1 have an orientation of 5°–10° (Figure 9d). The fiber orientation distribution of the Core layer and the Skin layer 1 are presented in Figure 9c, where the average values for the Core layer and the Skin layer 1 are 26°, and

13°, respectively. Through these quantitative visualizations, the image-based reconstruction allows spatial characterization of the SCFRP composite.

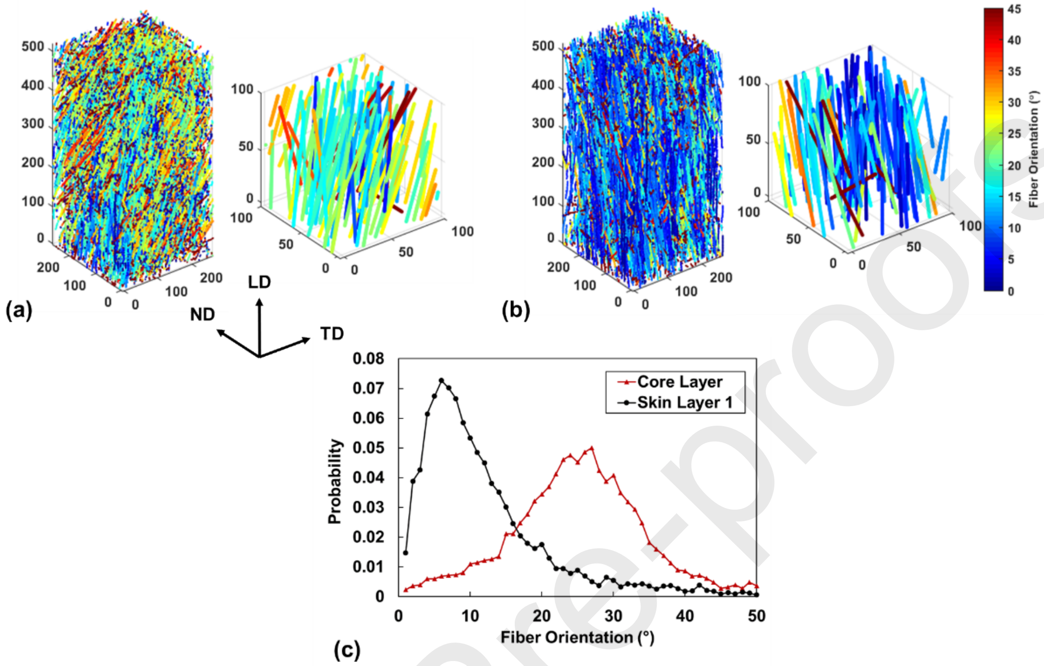

Figure 9. Representative color-coded reconstruction of fiber orientations for (a) Core Layer and (b) Skin Layer 1. (c) The fiber orientation distribution of the Core Layer and Skin Layer 1.

To compute the stiffness tensors for composites with straight fibers, only the fiber orientation tensor is required for the calculation. Using the PCA approach according to the coordinate system defined in Figure 6a, the second-order tensors of fiber orientations for the reconstructed volumes displayed in Figure 8 are:

$$\boldsymbol{a}_{2_{Skin\ layer\ 1}} = \begin{bmatrix} 0.83 & 0.01 & 0.02 \\ 0.01 & 0.07 & 0.00 \\ 0.02 & 0.00 & 0.10 \end{bmatrix}, \tag{10a}$$

$$\boldsymbol{a}_{2_{Core\ layer}} = \begin{bmatrix} 0.78 & -0.02 & -0.16 \\ -0.02 & 0.08 & 0.01 \\ -0.16 & 0.01 & 0.14 \end{bmatrix}, \tag{10b}$$

$$\boldsymbol{a}_{2_{Skin\ layer\ 2}} = \begin{bmatrix} 0.85 & -0.01 & 0.06 \\ -0.01 & 0.04 & 0.00 \\ 0.06 & 0.00 & 0.11 \end{bmatrix}. \tag{10c}$$

As indicated in the second-order orientation tensors, $\boldsymbol{a_2}$, the LD-LD component, $a_{LD\,LD}$ was 0.83, 0.78, and 0.85 for Skin layer 1, Core layer, and Skin layer 2, respectively, which is the largest value in the second-order tensor. Therefore, the fibers in the SCFRP composites provide the highest reinforcement in the LD direction. It should be noted that the orientation tensors of both skin layers are similar. The $a_{LD\,LD}$ from the $\boldsymbol{a_{2core\,layer}}$ was 0.78, which is less than in the skin layers. This implies that the core layer has a marginally smaller reinforcing efficiency in the LD than in the skin layers. The stiffness tensor for each cuboid was calculated by Eq. 9 for a given set of Young's modulus (E) and Poisson's ratios (ν), in which the superscript specifies the type of material (e.g., fiber), and the subscript specifies the directional property (e.g., LD). Here, E_{LD}^{fiber}, E_{LD}^{matrix}, are assumed to be 210 GPa, and 2.75 GPa, respectively, where the values were stated in [8]. ν^{fiber}, and ν^{matrix} are assumed to be 0.2 and 0.35, respectively, which are typical values for carbon fiber and PA 66 [33]. Assuming the diameter of the fibers is six voxels (i.e., 7.8 μm), the average fiber volume fractions of skin and core layers were determined as 0.291 ± 0.020 and 0.290 ± 0.019, respectively, which are statistically consistent with the pyrolysis experiment (i.e., 0.286 and 0.284) through the two-sample t-test with a significance level of 0.05, as reported in ref. [8]. The volume fraction calculated from the pyrolysis experiment was measured by weighing the mass of the sample before and after heating and using the following formulation:

$$V_f = \frac{m_f/\rho_f}{m_f/\rho_f \ + (m_o - m_f)/\rho_m}, \tag{11}$$

where m_o is the specimen's original mass, m_f is the specimen's final mass after the pyrolysis, ρ_f is the density of the carbon fiber, and ρ_m is the density of the matrix, Polyamide 66. To unveil the relationship between the microscale morphology and associated macroscale mechanical properties, Young's modulus for each layer can be computed by:

$$E_{LD} = \frac{C_{LD\,LD}C_{TD\,TD} - C_{LD\,TD}^2}{C_{TD\,TD}}, \tag{12}$$

where $C_{LD\,LD}$, $C_{TD\,TD}$, and $C_{LD\,TD}$ are $C_{LD\,LD\,LD\,LD}$, $C_{TD\,TD\,TD\,TD}$, and $C_{LD\,LD\,TD\,TD}$, respectively from the stiffness tensor [C_{ijkl}]. This resulted in an average E_{LD} of 20.98 GPa, 14.78 GPa, and 21.05 GPa for Skin layer 1, Core layer, and Skin layer 2, respectively. Additional quasi-static tensile tests according to ASTM D638-14 [29] were performed in the previous study [8], where Young's modulus of the Skin Layer was measured as 21.9 GPa and the value was 13.8 GPa for the Core Layer. The estimation errors of the proposed approach by comparing the experimental results were 4.20%, 7.10%, and 3.88% for Skin layer 1, Core layer, and Skin layer 2, respectively. Comparing to the estimation results reported in [8], the proposed framework provided a more accurate prediction than that of using classical laminate theory. Hence, the proposed framework provides a valid mechanical property estimation of the elastic modulus for an SCFRP composite with non-uniform fiber orientation using the non-destructive image-based technique.

3.2 Long CFRP(LCFRP) composite with curved fibers

For fiber systems with curved fibers, an LCFRP composite was examined, which was manufactured by BASF Corp. consisting of 40 wt% carbon fiber and PA66 as the polymer matrix. Each LCFRP composite sample was machined from an injection molded oil pan part as described in [33] and was cut to a dogbone shape with a gauge dimension of 6 ± 0.2 mm × 2.3 ± 0.1 mm × 2.4 ± 0.1 mm in LD, TD, and ND, respectively. The previous study concluded Young's modulus of studied samples was 29.3 ± 1.85 GPa [33]. The preliminary 2D μXCT image of the LCFRP composite, displayed in Figure 10, illustrates that the fiber orientations are distinctively different along the ND, implying a skin-core-skin structure. From visual observation, the majority of fibers in the core layer are aligned in the TD, whereas the specific orientation of the fibers in the skin layers requires in-depth characterization, as the 2D representations of the fibers in the skin layers are presented as ellipses with varied aspect ratios. Three individual cuboids were extracted with a size of 400 × 250 × 250 voxels (i.e., 0.520 mm × 0.325 mm × 0.325 mm) in the LD × TD × ND for fiber characterization and mechanical property prediction. Each cuboid from the same layer was extracted from the same width and thickness location, with different length locations (i.e., covering a length span of 1.56 mm). The size of the cuboids was limited in the ND due to the thickness of each layer, and the average thickness of Skin layer 1, Core layer, and Skin layer 2 was 0.878 mm, 0.435 mm, and 1.105 mm, respectively.

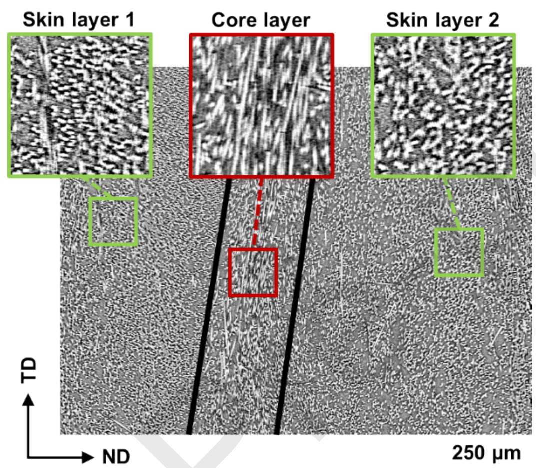

Figure 10. Representative 2D μXCT reconstruction of skin-core-skin structure in the TD/ND plane. Out-of-plane direction (i.e., LD) is the same as the direction of tensile loading.

A 3D reconstruction of each cuboid was employed with the proposed iterative template matching algorithm, where the reconstruction time was approximately 4 hours, and each reconstructed volume contained an average of 2093 ± 162 fibers. Each fiber was represented by the set of coordinates forming its centerline (e.g., Figure 11a). The fiber orientation and curvature vectors, $\vec{\boldsymbol{p}}$ and $\vec{\boldsymbol{q}}$, are defined according to the coordinate system illustrated in Figure 6b. For example, Figure 11a is a singular fiber with a curvature ratio of 0.80 and an orientation and curvature vector of $\vec{\boldsymbol{p}} = [0.90, 0.04, -0.44]$ and $\vec{\boldsymbol{q}} = [-0.36, 0.63, 0.69]$, respectively. Figures 11b–11d show the color-coded fiber centerlines with respect to fiber curvature ratio for Skin layer 1, Core layer, and the Skin layer 2, respectively. Representations of the fibers with low ($\eta = 0$), medium ($\eta = 0.2$), and high ($\eta = 0.5$) curvature ratios are presented in Figure 11e; these were extracted from the Skin layer 2. From Figures 11b–11d, no particular pattern is presented in the spatial distribution, and the average curvature ratio, $\overline{\eta}$, for Skin layer 1, Core layer, and Skin layer 2 is 0.280, 0.251, and 0.266, respectively. Hence, the presence of fiber curvatures in the LCFRP composite is confirmed. It is important to note that when two materials have the same orientation tensor, the material with smaller η (i.e., straighter fibers) has a larger stiffness modulus in the LD than the material with larger η. This implies that the elastic property in LD would be over-estimated if curvature is not considered.

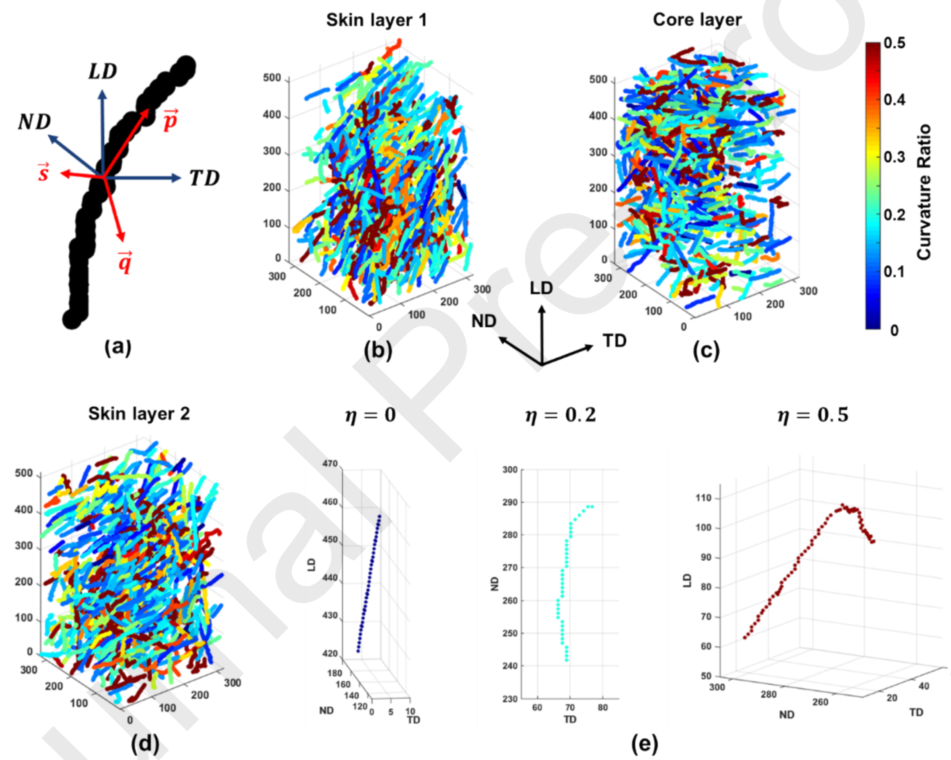

Figure 11. Representative reconstruction of LCFRP composite for (a) a single fiber, curvature ratio color-coded, (b) Skin layer 1, (c) Core layer, (d) Skin layer 2, and (e) representative fiber of $\eta = 0, 0.2,$ and 0.5 from Skin layer 2.

The fiber orientation and curvature tensors were then computed by summarizing all the fibers in a cuboid using Eqs. 3–6. The corresponding second-order orientation and curvature tensors of the reconstructed volumes displayed in Figure 12 are:

$$\boldsymbol{a}_{2_{skin\ layer\ 1}} = \begin{bmatrix} 0.69 & 0.19 & -0.06 \\ 0.19 & 0.17 & -0.03 \\ -0.06 & -0.03 & 0.14 \end{bmatrix},\ \boldsymbol{b}_{2_{skin\ layer\ 1}} = \begin{bmatrix} 0.15 & -0.12 & 0.03 \\ -0.12 & 0.48 & 0.01 \\ 0.03 & 0.01 & 0.37 \end{bmatrix} \tag{13a}$$

$$\boldsymbol{a}_{2_{core\ layer}} = \begin{bmatrix} 0.35 & -0.04 & 0.00 \\ -0.04 & 0.53 & 0.05 \\ 0.00 & 0.05 & 0.12 \end{bmatrix},\ \boldsymbol{b}_{2_{core\ layer}} = \begin{bmatrix} 0.33 & 0.02 & -0.03 \\ 0.02 & 0.26 & -0.05 \\ -0.03 & -0.05 & 0.41 \end{bmatrix} \tag{13b}$$

$$\boldsymbol{a}_{2_{skin\ layer\ 2}} = \begin{bmatrix} 0.49 & 0.04 & 0.01 \\ 0.04 & 0.41 & 0.01 \\ 0.01 & 0.01 & 0.10 \end{bmatrix},\ \boldsymbol{b}_{2_{skin\ layer\ 2}} = \begin{bmatrix} 0.28 & -0.03 & -0.01 \\ -0.03 & 0.35 & 0.01 \\ -0.01 & -0.04 & 0.37 \end{bmatrix}. \tag{13c}$$

As indicated in the second-order orientation tensors, $\boldsymbol{a_2}$, the LD-LD component, $a_{LD\ LD}$, in Skin layer 1 and 2 is 0.69 and 0.49, respectively, which is the largest value in each tensor, providing the highest reinforcement in the LD direction; whereas the largest tensor value in the core layer is $a_{TD\ TD} = 0.53$, indicating that the fibers in the core layers align with the TD axis. This trend is also observed in the reconstructed volumes, illustrated in Figure 12. It can be noted that the $a_{LD\ LD}$ and $a_{TD\ TD}$ components of Skin layer 2 are 0.49 and 0.41, respectively, and their difference (0.08) is considerably less than in Skin layer 1 (0.52) and Core layer (0.18), which indicates that the majority of the fibers in Skin layer 2 are aligned diagonally in the LD-TD plane (Figure 12c). In the curvature tensor, the $(b_{LD\ LD}, b_{TD\ TD}, b_{ND\ ND})$ for Skin layer 1 and 2 is (0.15, 0.48, 0.37) and (0.28, 0.35,0.37), respectively. $b_{TD\ TD}$ and $b_{ND\ ND}$ are the two largest values in the tensor, and their small differences indicate that the fiber curvature vectors in the skin layers align diagonally in the TD-ND plane, thereby providing reinforcement associated with fiber curvatures in the direction diagonally in the TD-ND plane. The diagonal values of the core layer curvature tensor are 0.33, 0.26, and 0.41, such that the curvature vectors in the core layer are aligned diagonally in the LD-ND plane.

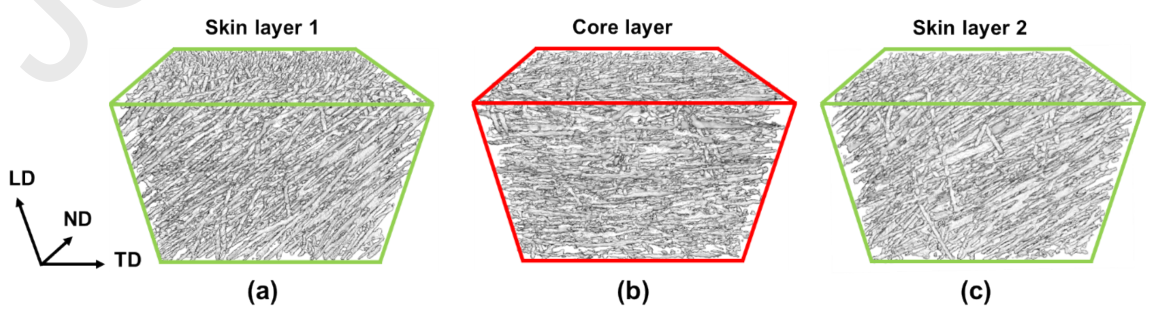

Figure 12. Representative reconstruction of LCFRP composite in (a) Skin layer 1, (b) Core layer, and (c) Skin layer 2.

To unveil the relationship of the microscale morphology of the LCFRP composites and its corresponding mechanical properties, Eq. 7 is used for computing the stiffness tensor of the extracted cuboids with the values of moduli and Poisson ratios of carbon fiber and polymer matrix, PA 66 reported in [33]. The fiber volume fraction of the LCFRP composite is set to be 30% converted from the fiber weight fraction of 40% [33]. To calculate the overall stiffness matrix of the material, the laminate analogy derived in [39] is adopted considering the layer thickness, which was estimated as the following:

$$A_{ij} = \sum_{g=1}^{G} C_{ij}^{g} a^{g}, \; i,j = LD, TD, ND, \tag{14}$$

where a^g is the thickness proportion of layer g, and G is the total number of layers (i.e., three in this case). The overall longitudinal modulus is estimated as:

$$E_{LD} = \frac{A_{LD\,LD} A_{TD\,TD} - A_{LD\,TD}^{2}}{A_{TD\,TD}}. \tag{15}$$

The thickness fraction of Skin layer 1, Core layer, and Skin layer 2 was measured as 36.3%, 18.0%, and 45.7%, respectively, by random sampling at multiple longitudinal locations of μXCT images. The calculated E_{LD} was 30.4 GPa, which is within the error margin of the experimental result from [33]. Without consideration of the curvature, the calculated E_{LD} would have been 32.56 GPa, which would lead to an overestimation. It is important to note that the proposed framework can estimate the longitudinal modulus for each layer as it is demonstrated for SCFRP composites; however, only the entire sample's longitudinal modulus is available for the validation of the LCFRP composites.

Furthermore, the localized E_{LD} was estimated by calculating the stiffness tensors of a smaller volume from the cuboid; Figure 13 illustrates the spatial distribution of the calculated E_{LD} of a cuboid extracted at the interface of Skin layer 1 and Core layer. Higher local E_{LD} values are located on the side of Skin layer 1, whereas lower local E_{LD} values are located on the side of the core layer owing to the different microscale morphologies in the skin and core layers. The gradual transition in the localized E_{LD} from the Skin layer 1 to the Core layer implies a gradual transition of the fiber orientation and curvature tensors. The image-based reconstruction approach allows spatial characterization of the fiber orientation and curvatures of an LCFRP composite thereby enabling the spatial characterization of the material property without the requirement for executing a time-consuming finite element analysis (FEA) simulation on the 3D model of the reconstructed geometry from the XCT.

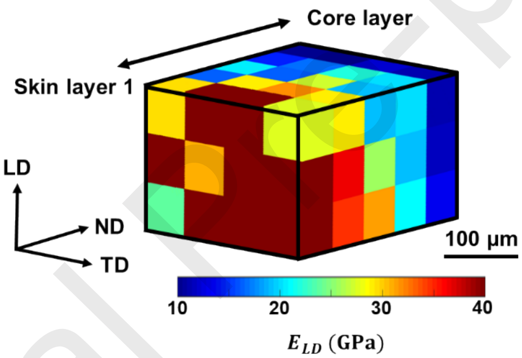

Figure 13. Spatial distribution of calculated E_{LD} for the skin–core interface

4. Conclusions

This study proposed a framework using image-based techniques to quantitatively analyze fiber characteristics for material mechanical property prediction of non-uniformly orientated fiber systems, i.e., injection-molded SCFRP and LCFRP composites. The internal microstructure was revealed through μXCT, implying a skin-core-skin structure for both materials. Quantitative fiber morphologies (i.e., fiber curvatures, orientation, length distributions) were characterized, and the curvature distributions indicated that the SCFRP composite contained straight fibers, whereas curved fibers were present in the LCFRP composite. Furthermore, the statistical and spatial characterizations of the fiber geometric properties provided essential microstructural data for material property calculation (i.e., stiffness tensor and Young's modulus). The proposed 3D image-based mechanical property prediction of Young's modulus yielded reliable and robust results for both SCFRP and LCFRP composites.

This research demonstrates that microstructural characterizations extracted from µXCT images can be implemented for spatial characterization and mechanical property predictions. The framework leverages the numerical image processing techniques and local fiber-tracking approach to account for non-uniformly orientated fiber systems with the straight or curved fibers. The statistical distributions of the extracted fiber centerlines are calculated using tensor representations with a configuration averaging approach, and the corresponding stiffness matrix and Young's modulus estimation of the material are evaluated by employing the Halpin–Tsai model and laminate analogy approach. The proposed framework provides a valid estimation of elastic properties with image-based microstructural analysis, which enables to replace the traditional FEA method.

Acknowledgment

The authors acknowledge the financial support from the Ford Motor Company and the ICS 2018 Seed Grant Program at Pennsylvania State University. Also, the authors thank the support received from Pavel D. Shevchenko from Argonne National Laboratory.

References

[1] P. Wright, X. Fu, I. Sinclair, S.M. Spearing, Ultra high resolution computed tomography of damage in notched carbon fiber-epoxy composites, J. Compos. Mater. 42 (2008) 1993-2002.

[2] P. Write, A. Moffat, I. Sinclair, S.M. Spearing, High resolution tomographic image and modeling of notch tip damage in a laminated composite, Comps. Sci. Technol. 70 (2010) 1444-1452.

[3] N.M. Larson, F.W. Zok, Insights from *in-situ* X-ray computed tomography during axial impregnation of unidirectional fiber beds, Compos. Part A. 107 (2018) 124-134.

[4] S. Pei, K. Wang, Y. Li, D. Zeng, X. Su, J. Li, H. Yang, X. Xiao, Spatiotemporal characterization of 3D fracture behavior of carbon-fiber-reinforced polymer composites, Compos. Struct. 203 (2018) 30-37.

[5] F. Cosmi, A. Bernasconi, N. Sodini, Phase contrast micro-tomography and morphological analysis of a short carbon fibre reinforced polyamide, Compos. Sci. Technol. 71 (2011) 23-30.

[6] A.E. Scott, I. Sinclair, S.M. Spearing, A. Thionnet, A.R. Bunsell, Damage accumulation in a carbon/epoxy composite: comparison between a multiscale model and computed tomography experimental results, Compos. Part A. 43 (2012) 1514-1522.

[7] M.W. Czabaj, M.L. Riccio, W.W. Whitacre, Numerical reconstruction of graphite/epoxy composite microstructure based on sub-micron resolution X-ray computed tomography, Compos. Sci. Technol. 105 (2014) 174-182.

[8] K. Wang, S. Pei, Y. Li, J. Li, D. Zeng, X. Su, X. Xiao, N. Chen, *In-situ* 3D Fracture Propagation of Short Carbon Fiber Reinforced Polymer Composites, Compos. Sci. Technol. 182 (2019) 107788.

[9] F. Gao, J.W. Patrick, A. Walker, The characterization of cracks and voids in two-dimensional carbon-carbon composites, Carbon. 31 (1993) 103-108.

[10] D.J. Bull, L. Helfen, I. Sinclair, S.M. Spearing, T. Baumbach, A comparison of multi-scale 3D X-ray tomographic inspection techniques for assessing carbon fibre composite impact damage, Compos. Sci. Technol. 75 (2013) 55-61.

[11] R. Seltzer, C. González, R. Muñoz, J. LLorca, T. Blanco-Varela, X-ray microtomnography analysis of the damage micromechanisms in 3D woven composites under low-velocity impact, Compos. Part A 45 (2013) 49-60.

[12] S.C. Wu, T.Q. Xiao, P.J Withers, The imaging of failure in structural materials by synchrotron radiation X-ray microtomography, Eng. Fract. Mech. 182 (2017) 127-156.

[13] P.J. Schilling, BP.R. Karedla, A.K. Tatiparthi, M.A. Verges, P.D. Herrington, X-ray computed microtomography of internal damage in fiber reinforced polymer matrix composites, Compos. Sci. Technol. 65 (2005) 2071-2078.

[14] L. Dong, H. Wadley, Mechanical properties of carbon fiber composite octet-truss lattice structures, Compos. Sci. Technol. 119 (2015) 26-33.

[15] W.K. Pratt, Digital Image Processing, fourth ed., Los Altos, California, 2007.

[16] D. Salaberger, K.A. Kannappan, J. Kastner, J. Reussner, T. Auinger, Evaluation of computed tomography data from fibre reinforced polymers to determine fibre length distribution, Int. Polym. Proc. 26 (2011) 283-291.

[17] S.C. Garcea, Y. Wang, P.J. Withers, X-ray computed tomography of polymer composites, Compos. Sci. Technol. 156 (2018) 305-319.

[18] M.J. Emerson, K.M. Jespersen, A.B. Dahl, K. Conradsen, L.P. Mikkelsen, Individual fibre segmentation from 3D X-ray computed tomography for characterising the fibre orientation in unidirectional composite materials, Compos. Part A, 97 (2017) 83-92.

[19] M.J. Emerson, Y. Wang, P.J. Withers, K. Conradsen, A.B. Dahl, V. A. Dahl, Quantifying fibre reorientation during axial compression of a composite T through time-lapse X-ray imaging and individual fibre tracking, Compos. Sci. Technol. 168 (2018) 47-54.

[20] P. J. Crevelinga, W. W. Whitacreb, M. W. Czabaja, A fiber-segmentation algorithm for composites imaged using X-ray microtomography: Development and validation, Compos. Part A 126 (2019) 105606.

[21] R.M. Sencu, Z. Yang, Y.C. Wang, P.J. Withers, C. Rau, A. Parson, C. Soutis, Generation of micro-scale finite element models from synchrotron X-ray CT images for multidirectional carbon fibre reinforced composites, Compos. Part A 91 (2016) 85-95.

[22] R.F. Agyei, M.D. Sangid, A supervised iterative approach to 3D microstructure reconstruction from acquired tomographic data of heterogeneous fibrous sytems, Compos. Struct. 206 (2018) 234-246.

[23] P.A. Hessman, T. Riedel, F. Welschinger, K. Hornberger, T. Böhlke, Microstructural analysis of short glass fiber reinforced thermoplastics based on x-ray micro-computed tomography, Compos. Sci. Technol. 183 (2019) 107752

[24] N. Naouar, E. Vidal-Salle, J. Schneider, E. Maire, P. Boisse, 3D composite reinforcement meso F.E. analyses based on X-ray computed tomography, Compos. Struct. 132 (2015) 1094-1104.

[25] R. Sharma, P. Mahajan, R.K. Mittal, Fiber bundle push-out test and image-based finite element simulation for 3D carbon/carbon composites, Carbon 50 (2012) 2717-2725.

[26] M. Huang, Y-M Li, X-ray tomography image-based reconstruction of microstructural finite element mesh models for heterogeneous materials, Comput. Mater. Sci 67 (2013) 63-72.

[27] R. Hill, Theory of mechanical properties of fiber-strengthened materials: I. elastic behavior, J. Mech. Phys. Solids, 12 (1964), 199-212.

[28] Z-M. Huang, Micromechanical prediction of ultimate strength of transversely isotropic fibrous composites, Int. J Solids. Struct., 38 (2001) 4147-4172.

[29] B.N. Ngytebm S.K. Bapanapalli, J.D. Holbery, M.T. Smith, V. Kunc, B.J. Frame, J.H. Phelps, C.L. Tucker III, Fiber length and orientation in long-fiber injection-molded thermoplastics – part I: modeling of microstructure and elastic properties, J. Compos. Mater. 42 (2008) 1003-1029.

[30] V. Kunc, S.W. Case, H.J. Santos-Villalobos, S. Simunovic, The stiffness tensor for composites with curved discontinuous fibers, Compos. Part A 72 (2015) 239-248.

[31] ASTM D638-14. Standard test method for tensile properties of plastics, ASTM International, West Conshohocken, PA, 2014.

[32] M. Teβmann, S. Mohr, S. Gayestkyy, U. Haβler, R. Hanke, GT. Greiner, Automatic determination of fiber-length distribution in composite material using 3D CT data, EIRASIP J. Adv. Signal Process. 2010 (2010):545030.

[33] Y. Li, M. Shewey, L. Su, K. L, P. Tibbenham, D. Zeng, Prediction and validation of anisotropic elastic property of injection molded PA66/carbon fiber composites parts for automotive applications, Proceedings of the American Society for Composites—Thirty-second Technical Conference: 10.12783/asc2017/15193.

[34] D. Gürsoy, F.D. Carlo, X. Xiao, C. Jacobsen, TomoPy: a framework for the analysis of synchrotron tomographic data, J Synchrotron Radiat. 21 (2014) 1188–93.

[35] N. Otsu, A threshold selection method from gray-level histograms, IEEE Trans. Syst. Man. Cybern. 9 (1979) 62-66.

[36] K. Briechle, U.D. Hanebeck, Template matching using fast normalized cross correlation, Proc. SPIE Int. Soc. Opt. Eng. 4387(2001) 95-102.

[37] S. Mori, P.C.M. Zijl, Fiber tracking: principles and strategies – a technical review, NMR Biomed. 15 (2002) 468-480.

[38] S.G. Advani, C.L. Tucker III, The use of tensors to describe and predict fiber orientation in short fiber composites, J. Rheol 31 (1987) 751-784.

[39] J.C. Halpin, J.L Kardos, Strength of discontinuous reinforced composites: I. fiber reinforced composites, Polym Eng Sci 16 (1978) 496-504.

[40] J.C. Halpin, J.L. Kardos, The Halpin-Tsai Equations: A Review, Polym Eng Sci 16 (1976) 344-352.

August 20th, 2019

Dear Dr. Advani,

Authors declares that there are no conflicts of interest.

Sincerely Yours,

Jingjing Li, Ph.D.
Associate Professor
Department of Industrial and Manufacturing Engineering
310 Leonhard Building, The Pennsylvania State University, University Park, PA 16802
Phone: 814-863-1300
Email: jul572@psu.edu

Credit Author Statement

Shenli Pei: Methodology, Validation, Writing-original draft;

Kaifeng Wang: Investigation, Writing-original draft;

Jingjing Li: Funding acquisition, Conceptualization, Supervision, Writing- review & editing;

Yang Li: Investigation, Writing- review & editing;

Danielle Zeng: Funding acquisition, Supervision, Writing- review & editing;

Xuming Su: Funding acquisition, Supervision, Writing- review & editing;

Xianghui Xiao: Writing- review & editing;

Hui Yang: Writing- review & editing.